Enhanced global dust counteracted greenhouse warming during the mid- to late-Holocene

Shiwei Jiang [1], Xin Zhou [1]*, Jasper F. Kok [2], Qifan Lin [3], Yonggang Liu [3], Tao Zhan [4], Yanan Shen[1], Zhibo Li [5], Xuanqiao Liu [1], Anze Chen [1], Luo Wang [6], Wen Chen [7], John P. Smol [8], Zhengtang Guo [6, 9]

1 School of Earth and Space Sciences, University of Science and Technology of China, Hefei, China.

2 Department of Atmospheric and Oceanic Sciences, University of California-Los Angeles, Los Angeles, USA.

3 Laboratory for Climate and Ocean-Atmosphere Studies, Department of Atmospheric and Oceanic Sciences, School of Physics, Peking University, Beijing, China.

4 General Institute of Ecological Geology Survey and Research of Heilongjiang Province, Harbin, China.

5 Regional Climate Group, Department of Earth Sciences, University of Gothenburg, Gothenburg, Sweden.

6 Institute of Geology and Geophysics, Chinese Academy of Sciences, Beijing, China.

7 Department of Atmospheric Sciences, Yunnan University, Kunming, China.

8 Paleoecological Environmental Assessment and Research Lab, Department of Biology, Queen's University, Kingston, Canada.

9 CAS Center for Excellence in Life and Paleoenvironment, Beijing, China.

*Corresponding author: Xin Zhou (xinzhou@ustc.edu.cn)

Abstract

Known as the "Holocene temperature conundrum", controversy remains between paleoclimate reconstructions indicating cooling during the late-Holocene versus model simulations indicating warming. Here, we present a composite Holocene winter temperature index record derived from East Asian winter monsoon (EAWM) reconstructions. This new temperature index record documents a thermal maximum occurring during the mid-Holocene, followed by a cooling trend. Along with other Holocene winter temperature reconstructions, these findings collectively indicate a cooling trend during the late-Holocene, consistent with global annual average temperature reconstructions. Notably, our composite dust records and dust sensitivity simulations identified enhanced global aeolian dust, which has been overlooked in previous model simulations, as a likely driver of the cooling trend throughout the mid- to late-Holocene. Our new evidence does not support the current seasonal bias explanation of the Holocene temperature controversy, but rather suggests potential mechanisms that could help explain the differences between temperature inferences from models and paleo-reconstructions in the past.

Keywords

Holocene temperature conundrum; Global aeolian dust; East Asian winter monsoon; Holocene Thermal Maximum; Greenhouse gases warming

1. Introduction

A more complete understanding of Holocene temperature changes and their possible driving mechanisms are required for a better understanding of future global climate change (Kaufman et al., 2023). Multiproxy reconstructions have shown a pronounced cooling trend following the mid- to late-Holocene (Marcott et al., 2013; Kaufman et al., 2020; Zhang et al., 2022), with a Holocene Thermal Maximum (HTM) at ~10–6 ka BP. The HTM has been considered a possible analog for future global warming (Badgeley et al., 2018; Curran et al., 2018). However, climate model simulations have shown a long-term global annual mean warming trend throughout the Holocene, primarily driven by glacial retreat and rising greenhouse gases (Liu et al., 2014; Barder et al., 2020; Bova et al., 2021; Osman Bova et al., 2021). This contradiction between reconstructions and model simulations of the trend of temperature changes during the Holocene is known as the "Holocene temperature conundrum" (Liu et al., 2014) and remains unresolved.

The seasonality of temperature proxy reconstructions has been proposed as a likely reason for the contradictions between reconstructed cooling and simulated warming during the late Holocene (Liu et al., 2014; Bova et al., 2021). This is because some temperature proxy indicators (such as pollen and chironomids) are primarily controlled by temperature during the growing season (i.e., the warm season), which depicts warm-season temperatures rather than annual average temperatures (Liu et al., 2014). However, changes in surface processes during the Holocene (such as aeolian dust and vegetation cover) and their significant climatic effects have been neglected in previous transient model simulations, which may also be the reason for the inconsistency between the modeled and reconstructed temperature trends (Liu et al., 2018; Tompson et al., 2022). Robust seasonal (particularly winter) temperature reconstructions are essential for evaluating seasonal biases in proxy indicators and optimizing model simulations, thereby providing insights into the "Holocene temperature conundrum" (Zhang et al., 2022).

Most previous seasonal temperature reconstructions are based on the different responses of proxies (such as snails and pollen) (Dong et al., 2022; Zhang et al., 2022) to the cold and warm seasons for seasonal signal recognition and separation, while there are few independent seasonal temperature reconstructions. Moreover, most available winter temperature records are from Europe and North America (Baker et al., 2017; Meyer et al., 2015; Kaufman et al., 2020), with fewer winter temperature reconstructions for other parts of the world, such as East Asia (Dong et al., 2022).

The East Asian winter monsoon (EAWM) is an atmospheric circulation in East Asia with evident seasonal characteristics and has a large impact on the winter weather and climate of the Asia-Pacific region (Wang et al., 2006). Observational data showed a strong link between the EAWM and winter temperature anomalies in East Asia on decadal scales (Zhang et al., 2012; Ding et al., 2014). Specifically, a stronger EAWM temporally coincides with negative winter temperature anomalies (cooler), while a weaker EAWM coincides with positive winter temperature anomalies (warmer) (Ding et al., 2014). Furthermore, simulation and reconstruction records have shown that the negative correlation between the EAWM and winter temperature remains close and stable on both century and millennium timescales (Ge et al., 2010; Liu et al., 2014; Liu et al., 2016; Kang et al., 2018; Zhang et al., 2019; Shi et al., 2022). Collectively, this suggests that changes in the EAWM is a powerful approach for inferring trends of Holocene winter temperature changes in East Asia.

In this study, we synthesized a winter temperature index record by integrating various proxy-reconstructed East Asian winter monsoon records. This record reflects the trends in Holocene East Asian winter temperature changes from the perspective of seasonal atmospheric circulation. It enables us to evaluate the reliability of the "seasonal bias hypothesis" of the "Holocene temperature conundrum". We then integrated global dust records to explore the potential effects of dust in the contradictions between the reconstructions and model simulations during the late

Holocene. Our findings offer a valuable perspective for optimizing climate models and addressing the “Holocene temperature conundrum”.

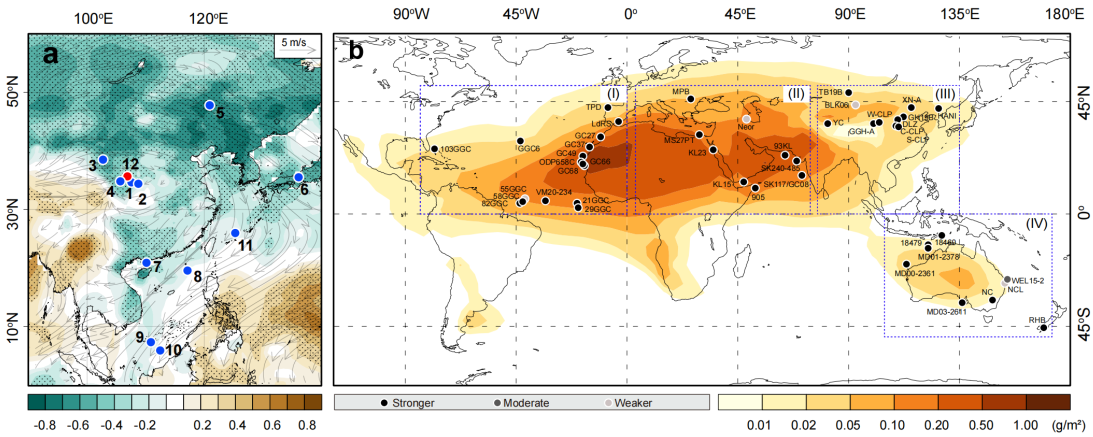

Fig. 1 Study area and site locations. (a) Map showing the location of collected EAWM (blue circles) and winter temperature (red circle) records (Table. 1). The grey lines and arrows indicate surface wind speed and direction during winter based on the NCEP/NCAR reanalysis data (Kalnay et al., 1996), while the shading indicates correlation of the instrumental winter temperature (Rayner et al., 2003; Fan and van den Dool, 2008) and the EAWM index (Chen et al., 2000) since 1979 CE; values exceeding the 95% confidence level are stippled. **(b)** Sites of dust records in the main dust source regions (Table 2). Records of stronger dust during the mid- to late-Holocene are indicated by black symbols, while those of weaker dust are indicated by grey symbols. The shading shows annual-mean present-day dust loading (Liu et al., 2018), which indicates the main dust source region.

2. Data and methods

2.1. EAWM records collection and stack

To overcome the limitations of inferring trend changes in East Asian winter temperature from single-site winter monsoon records, we collected different available winter monsoon records across East Asia based on the following criteria: (1) the study site must be located in a region where winter monsoon and winter temperature are positively correlated (Fig. 1a); (2) each record must span a sufficiently long period to cover the early, middle, and late Holocene; (3) the average temporal resolution during the Holocene must be <500 years; (4) records from the same site must use the most recently published data; (5) the winter monsoon indicators must be clearly defined, with proxies explicitly described as indicating winter monsoon in the original literature. A total of 11 records met these criteria and were included in the analysis (Table 1).

We first normalized the EAWM records to the standard Z-score, the standardized formula is as follow:

$$Z = (X - V)/SD$$

where X is the original value, V and SD are the average and standard deviation of the dust time series, and Z is the normalized result.

To mitigate the impacts of resolution disparities among different records on the winter temperature record, each EAWM record was standardized by calculating the mean value for every 500 years. Then, based on the inverse relationship between the EAWM and winter temperature, the standardized EWAM data were multiplied by −1 to generate the winter temperature index. Boxplots were then generated for each 500-year interval, and the composite East Asian winter temperature index record was fitted to the boxplots using locally weighted regression (LOESS). Please note that the EAWM is essentially the northwesterly wind controlled by the Siberian High (An et al., 1991; Xiao et al., 1992; Sun et al., 2012), prevailing throughout the winter half-year (December to May). Therefore, the winter temperature index developed from EAWM records in this study reflects a broader "winter temperature," referring to the temperature of the winter half-year or the cold-season temperature.

2.2. Dust records collection, classification, and stack

To study changes in global dust during the Holocene, available paleo-dust records were collected based on the following criteria: (1) study sites must be located in the main dust source regions; (2) the chronology of each record must be sufficient to identify the mid-Holocene and late-Holocene periods; and (3) the average temporal resolution must be <2000 years. A total of 45 records satisfied the above criteria and were therefore included in the analysis (Table 2).

The classification method for the trend of dust strength for each record during the Holocene was as follows: (1) the mean value for the late-Holocene (4–1 ka BP) and the mid-Holocene (7–4 ka BP) were calculated separately to represent the mean level of dust in the different periods and to avoid the influence of extreme values on the entire time series; (2) the standard deviation (σ) was calculated for each Holocene dust record; (3) the mean values of the late-Holocene (M_{lat}) and mid- Holocene (M_{mid}) were compared; (4) if the M_{lat} is higher (lower) than the M_{mid} and exceeded 0.1σ, the dust strength for the late-Holocene was classified as "stronger (weaker)." If the difference between M_{lat} and M_{mid} was within 0.1σ, the dust strength for the late-Holocene was classified as "moderate."

Paleo-dust records for each main dust source region were first normalized to the standard Z-score and stacked into a regional dust record. The standardized formula is described in the previous section. Locally weighted regression (LOESS) was applied to estimate long-term changes in dust for each region.

2.3. Dust simulation experiments

Dust simulations were conducted using a coupled climate model, the Community Earth System Model version 1.2.2 (CESM1.2.2), with the atmosphere-land-coupled version. The atmospheric (Community Atmosphere Model version 4, CAM4; Neale et al. 2013) and land (Community Land Model version 4, CLM4; Lawrence et al. 2012) components shared the same horizontal grid (f19) with a resolution of 1.9°(zonal) × 2.5° (meridional). The atmosphere has 26 vertical layers. For the simulations, the climatological monthly mean sea surface temperature and sea ice conditions were prescribed using the default distribution provided by the model (Hurrell et al., 2008).

The simulations were conducted for two periods, namely 6 ka and PI; the CO_2 concentrations were set to 263 and 280 ppm, respectively (Köhler et al., 2017). To simplify the simulations and reduce unnecessary complexity, aerosols were prescribed in the model, including dust mass mixing ratios in the atmosphere and dust deposition rates (Neale et al. 2013). The radiative effect of dust is highly uncertain, primarily due to interactions with clouds that current models do not consider. Previous studies have also found that the radiative effect of longwave radiation is considered to be local and limited relative to shortwave radiation, due to the global average shortwave effect being much greater than the longwave effect at both the top and surface of the atmosphere (Choobari et al. 2014; Albani et al. 2014; Liu et al., 2018). Therefore, to assess the validity of our hypothesis positing increased dust as a driver of the cooling trend during the mid-to-late-Holocene, we simulated a dust-induced cooling impact at the upper limit of existing constraints on dust's radiative effect (Kok et al., 2023), intentionally excluding warming from longwave interactions. For similar reasons, the dust content for the 6 ka was set as 0, and the PI value was set according to Mahowald et al. (2006).

3. Results and Discussion

3.1. Holocene EAWM evolution linked to winter temperature

Ten EAWM reconstructions (Table 1) indicate a weakening trend during the early-Holocene and a strengthening trend during the late-Holocene, with a notable shift occurring in the mid-Holocene. Among the proxies used for these EAWM reconstructions, loess grain size is considered to potentially be influenced by the expansion of dust source areas resulting from a weakening East Asian Summer Monsoon (EASM) (Yang and Ding, 2008; Yang et al., 2015). However, during the late-Holocene, when coarse loess grain size indicates an intensification of the EAWM (Li & Morrill, 2014; Xia et al., 2014; Kang et al., 2020), the intensity of the EASM continued to increase (Dykoski et al., 2005). Therefore, the influence of the EASM on loess grain size during the late-Holocene can be excluded.

Even though the timing of these shifts varies slightly among the records, we hypothesize that these discrepancies arise from differences in the resolution and chronological frameworks of the reconstructions. Only one record, that from northeastern China, diverges significantly, showing a continuous strengthening of the winter monsoon throughout the Holocene (Wu et al., 2019). However, the late-Holocene strengthening observed in this record is consistent with the other records. Overall, the trends of the EAWM reconstructions over millennial to multi-millennial timescales are consistent. The mean index of winter monsoon variability, synthesized from standardized records, indicates a decrease in EAWM intensity from the early to mid-Holocene, followed by a subsequent increase (Fig. 2a). Although this result differs from the continuous weakening of the Holocene EAWM shown by previous TRACE21 simulations (Wen et al., 2016), the phenomenon of strengthened EAWM during the late-Holocene has received support from the latest simulations (Zhou et al., 2023).

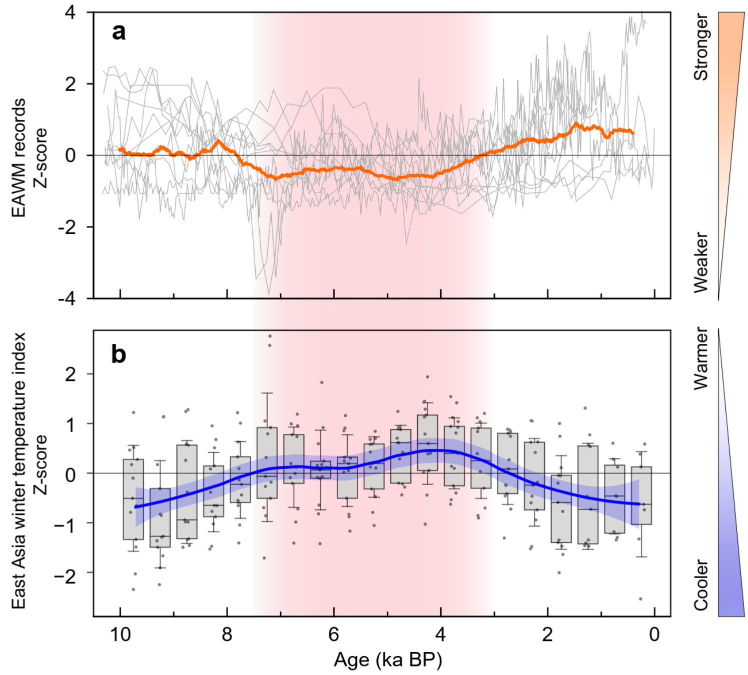

Fig. 2 EAWM records and the East Asia winter temperature index record. (a) The mean index of winter monsoon variability (orange line) and 11 EAWM records (gray lines). The EAWM records were first normalized to the standard Z-score and stacked into a composite record. (b) Holocene winter temperature index record (blue line) synthesized from EAWM records. The 500-year interval standardized EAWM data (black dots) are overlain with the results of the application of a smoothing function (LOESS), with bootstrapped 95% confidence intervals indicated by light blue shading. The red shading indicates the weaker EAWM and warmer interval.

Previous studies revealed a significant negative correlation between the EAWM and winter temperatures in East Asia over the past few decades, which was attributed to changes in the Siberian High (Ding et al., 2014). Reduced winter temperatures in East Asia strengthen the Siberian High, thereby increasing the pressure gradient between East Asia and the Northwest Pacific, which ultimately strengthens the EAWM. Conversely, increased winter temperatures in East Asia weaken EAWM via a decreased land-sea pressure gradient (Wang, 2006). A cooler winter temperature from ~1950 to 1985 CE was associated with a stronger EAWM, while warmer winter temperature was associated with a weaker EAWM from ~1985 to 2000 CE (Fig. S1) (Ding et al., 2014). The link between the EAWM and winter temperature was also demonstrated by paleoclimate datasets and climate models on century (Fig. S2) and millennial timescales (Fig. S3) (Ge et al., 2003; Liu et al., 2014; Liu et al., 2016; Kang et al., 2018; Zhang et al., 2019; Shi et al., 2022).

3.2. A Holocene winter temperature derived from EAWM.

As evidenced by the strong connection between the Siberian High-dominated EAWM and winter temperature, East Asian winter temperature significantly influences the EAWM. Consequently, we suggest that the EAWM, which shows a weakening trend in the early Holocene and a strengthening trend in the late Holocene, serves as a reliable indicator of millennial to multi-millennial variations in winter temperature. Considering the impacts of resolution disparities among different EAWM records on winter temperature index, we standardized each EAWM record by calculating the average value for every 500-year interval. The standardized EAWM data were then used to fit the Holocene East Asian winter temperature index record (Fig. 2b), allowing us to infer trends in winter temperature changes throughout the Holocene.

The winter temperature index record has three distinct millennial-scale phases over the Holocene (Fig. 2b). Negative Z-scores from 10 to 7.5 ka and 3 ka to preindustrial era imply a cooler winter temperature, whereas positive Z-scores from 7.5 to 3 ka imply a warmer winter temperature (Fig. 2b). The increase in the winter temperature index records from the early to mid-Holocene implies a warming trend, whereas the decreased of index value from the mid to late-Holocene implies a cooling trend. The winter temperature index record derived from the EAWM reconstruction was characterized by a maximal winter temperature during the mid-Holocene, followed by a cooling trend during the late-Holocene (Fig. 2).

To further assess the reliability of our winter temperature index record, we compared it to previous winter temperature reconstructions based on mollusks in East Asia (Dong et al., 2022), Northern Hemisphere (NH) marine data, and terrestrial multiproxy stacks (Kaufman et al., 2020) (Fig. 3a) over the Holocene, respectively. Our winter temperature index time series is consistent with the time series of winter temperatures based on the mollusk and NH multiproxy stacks (Fig. 3a). The negative Z-scores of our index that correspond with cooler winter temperature obtained based on mollusks in East Asia (Dong et al., 2022) and the negative Z-scores of NH multiproxy stacks (Kaufman et al., 2020) imply cooler conditions during the early-Holocene and late-Holocene. Conversely, the positive Z-scores during the mid-Holocene imply warmer winter temperatures (Fig. 3a). These records collectively show a gradually increasing trend in winter temperatures that occurred during the early- to mid-Holocene (before ~5 ka BP) and a gradually increasing trend since the mid-Holocene (after ~5 ka BP) (Fig. 3a). Therefore, we propose that the winter temperature index record derived from the EAWM reconstruction can be used to infer changes in long-term trends of Holocene winter temperatures.

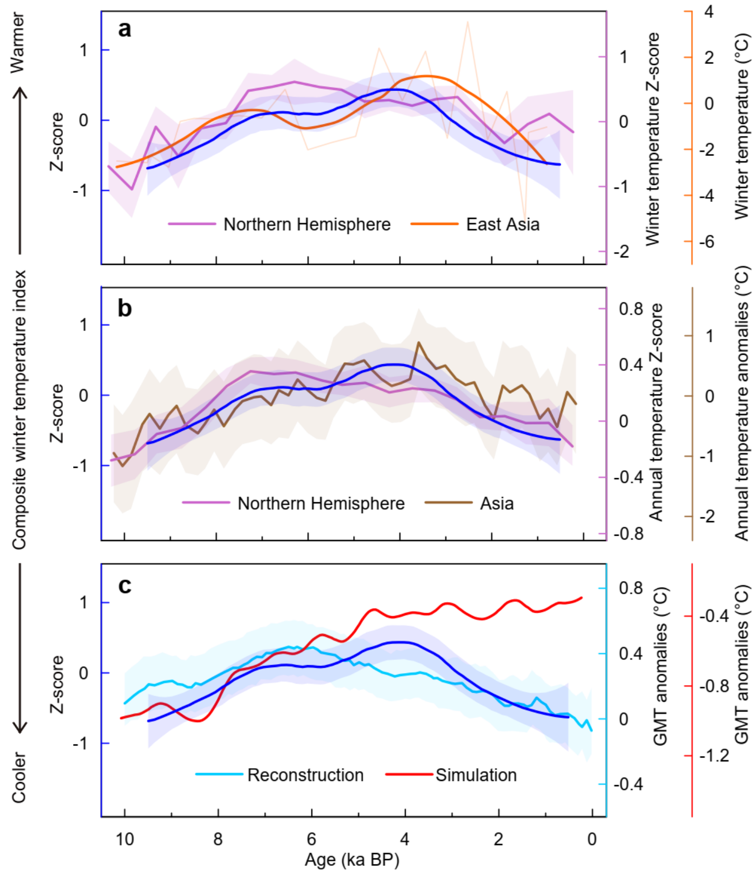

Fig. 3 Comparison between the Holocene winter temperature index record obtained in this study and other Holocene temperature records. The Holocene winter temperature index record from this study is plotted in each panel with a dark blue line. (a) Reconstructed winter temperature records based on mollusks from the loess section in East Asia (orange line) (Dong et al., 2022), and global winter temperature trends based on marine and terrestrial multiproxy stacks (purple line) (Kaufman et al., 2020). (b) Northern Hemisphere (NH) annual temperature trends based on marine and terrestrial multiproxy stacks (purple line) (Kaufman et al., 2020), and Asian annual temperature trends from pollen-based reconstructions (brown line) (Zhang et al., 2022). (c) Median global mean temperature (GMT) from three T12K individual reconstructions (light blue line) (Kaufman et al., 2020; Thompson et al., 2022), and simulated GMT anomalies obtained via the TraCE-21ka experiment (red line) (Liu et al., 2009; 2014). The shading indicates 95% uncertainty bands except for T12K (±1SD).

Our new Holocene winter temperature index record offered the possibility to assess the “seasonal bias hypothesis” which has previously been used to explain the “Holocene temperature conundrum”. The Holocene temperature reconstructions with the HTM pattern may indicate that summer temperatures, but not mean annual temperatures (as these proxies are primarily controlled by the temperature of the growing season in summer), may be related to the proxy-model mismatch (Liu et al., 2014). However, our record shows that the Holocene winter temperature changes followed the HTM pattern, and these changes were consistent with annual temperature reconstructions based on pollen records from East Asia (Zhang et al., 2022), NH and global multiproxy stacks (Kaufman et al., 2020) (Figs. 3b and c), but were inconsistent with the model simulated results, especially during the late-Holocene (Fig. 3c). Therefore, our new record and other winter temperature reconstructions (Kaufman et al., 2020; Dong et al., 2022) collectively suggest that seasonal biases of the reconstructions cannot explain the "Holocene temperature conundrum". Instead, these findings raise the possibility that another cooling forcing factor has been overlooked in model simulations, resulting in a warming trend in the model that does not match the cooling trend reconstructed during the mid- to late-Holocene. Therefore, focusing on additional temperature forcing factors that are ignored by the model may provide novel insights into optimizing the current climate model and resolving the "Holocene temperature conundrum".

3.3. Possible reasons for the "Holocene temperature conundrum"

Paleo-dust records in stratigraphic materials have shown that dust is an important factor affecting the radiative balance of the Earth (Maher et al., 2010) through various mechanisms, including interactions with radiation, clouds, atmospheric chemistry, and the cryosphere (Maher et al., 2010; Arimoto, 2001; Sassen et al., 2003; Boucher et al., 2000). Recent studies have further shown that enhanced dust has decreased the global mean effective radiative forcing since pre-industrial times, which has partly counteracted global warming (Stevens, 2015; Kok et al., 2017; 2023). Here, we attempt to develop this concept further as a possible forcing mechanism for cooling during the mid- to late-Holocene. The temperature effects of dust have rarely been discussed in previous studies on the “Holocene temperature conundrum” (Kaufman et al., 2023), likely owing to the lack of systematic analyses of Holocene global dust record changes and their possible climatic effects.

To test our hypothesis, we compared the winter (annual) temperature record with Holocene dust reconstructions from East Asia (Fig. 4). The results show that the trend of continuous cooling in East Asian winter (annual) temperatures during the late-Holocene corresponds well with enhanced East Asian dust (Fig. 4). This phenomenon supports our hypothesis and highlights the significant potential of global dust changes in addressing the “Holocene temperature conundrum”.

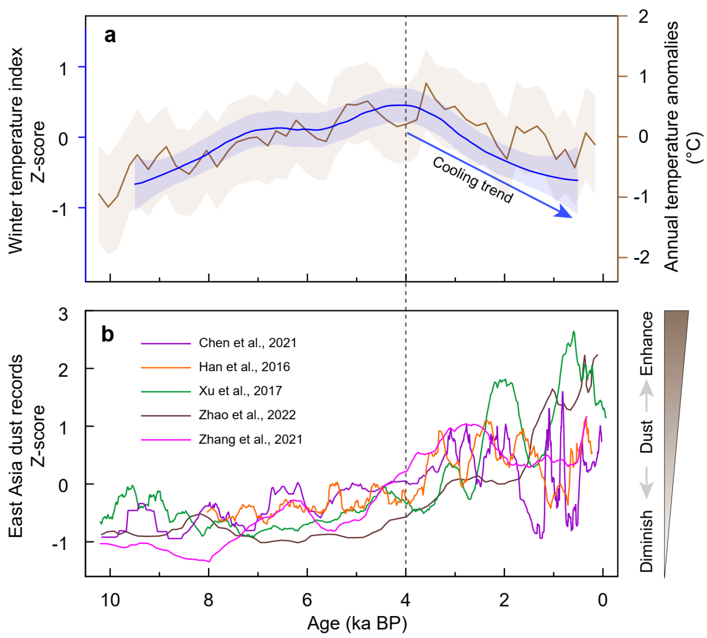

Fig. 4 Comparison of time series of our composite winter temperature index record with dust reconstructions in East Asia. (a) Holocene winter temperature index record synthesized from EAWM records (this study, blue line) and Asian annual temperature trends from pollen-based reconstructions (brown line) (Zhang et al., 2022). (b) Eolian activity record from Lake Xiarinur (green line) (Xu et al., 2017), dust storm record from the YC section (orange line) (Han et al., 2019), aeolian activity reconstruction based on grain size from Tolbo Lake (pink line) (Zhang et al., 2022), reconstructed Asian dust storm history from Lake Gonghai (purple line) (Chen et al., 2021), Holocene dust accumulation rate stack for the Chinese Loess Plateau (brown line) (Zhao et al., 2022).

To reconcile the Holocene temperature trend contradiction between reconstruction and model simulations from the perspective of climate effect of dust, we collated 44 dust records from 4 main dust source regions (i.e., the North Atlantic, Middle East, East Asia, and Australia; Fig. 5 and Table 2) to infer changes in global dust during the Holocene. Remarkably similar patterns of Holocene dust changes were observed in each stacked dust record from the four main dust source regions (Fig. 5). Collectively, these results indicate a coherent intensification of global dust since the mid-Holocene (~6–5 ka BP). In addition, the Na^{+} concentration record from Siple Dome ice cores (Mayewski and Maasch, 2006) also indicates some enhancement of dust during the mid- to late Holocene, although it is not as obvious as the dust records from primary dust source regions.

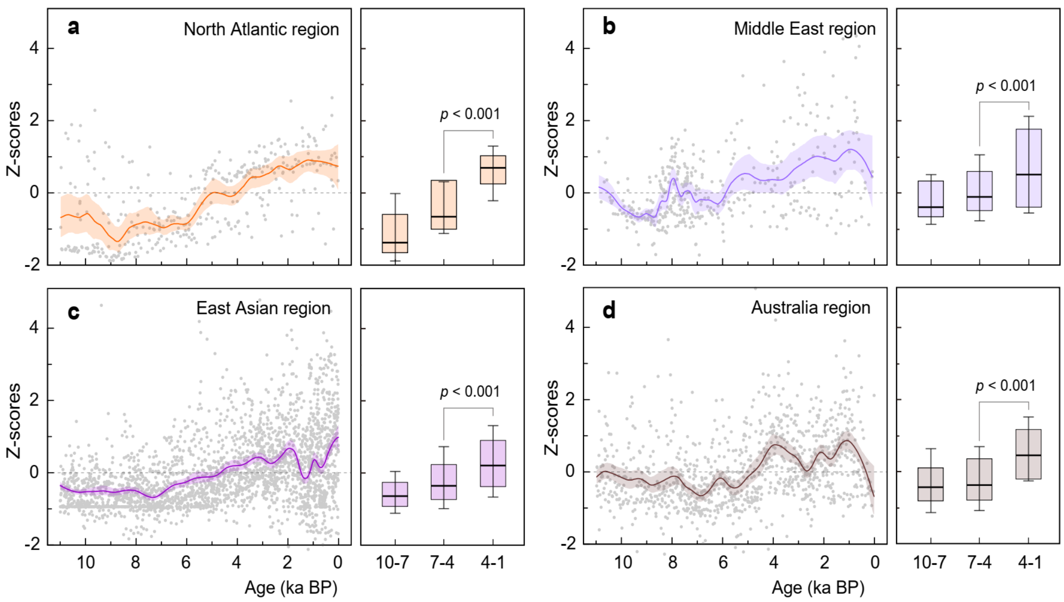

Fig. 5 Holocene dust records from the four dust core regions. (a) North Atlantic region, (b) Middle East region, (c) East Asia region, and (d) Australia region (Fig. 1b and Table 2). The raw dust data are overlain with the results of the application of a smoothing function (LOESS), with bootstrapped 90% confidence intervals indicated by orange shading. Box plots of dust strength for each 3-ka interval over the Holocene are shown in the right side of each panel.

We then compared our composite global dust records with Holocene temperature records from reconstruction and simulation data, and found that the mid- to late-Holocene, for which reconstructed and simulated temperature diverge, was characterized by significantly enhanced global dust after ~6 ka BP (Fig. 6), coincident with the cooling trend recorded in temperature reconstructions (Kaufman et al., 2020; Tompson et al., 2022) (Fig. 6), although glacial retreat (Dyke, 2004) and rising greenhouse gases (Köhler et al., 2017) had a warming effect during this period (Fig. 6b). Previous studies on the relationship between dust and temperature have found that, on glacial-interglacial timescales, temperature decreases may lead to more frequent dust activity (Lambert et al., 2008). However, recent research suggests that during the Holocene, factors other than temperature, such as human activities in East Asia (Chen et al., 2020; Chen et al., 2021) and the termination of the North African Green Sahara (Griffiths et al., 2020), may have been more influential drivers of dust activity, contributing to the global increase in dust levels during the late-Holocene. Therefore, we propose that increased dust was a significant factor driving late-Holocene cooling, which may have been overlooked by model simulations, thereby contributing to the model-proxy temperature inconsistency.

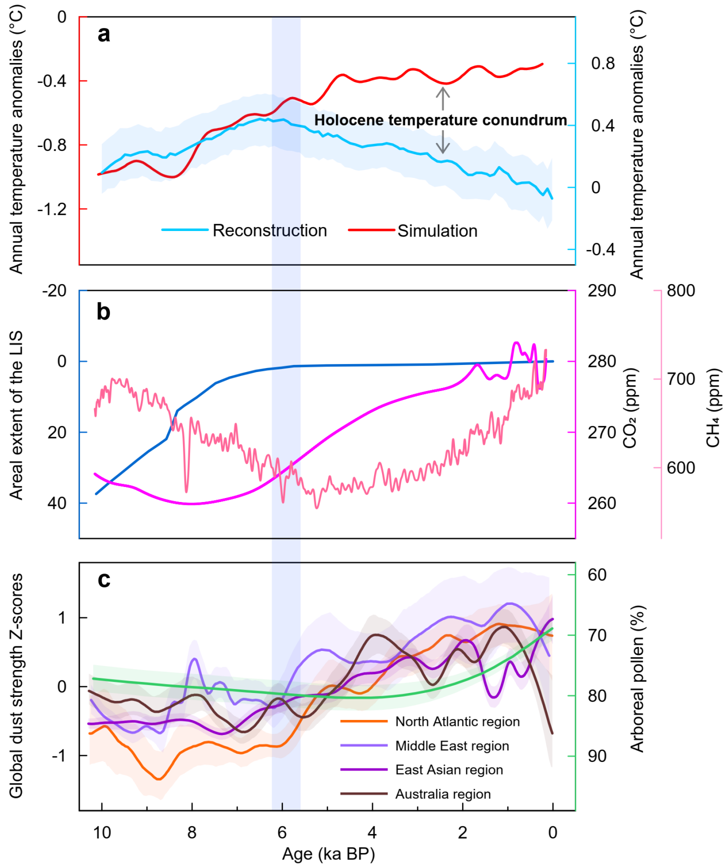

Fig. 6 Comparison of time series of Holocene temperature with possible forcing mechanisms. (a) Comparison of Holocene temperature reconstructions (light blue) (Kaufman et al., 2020; Tompson et al., 2022) and simulations (red) (Liu et al., 2014). (b) Concentrations of atmospheric greenhouse gases (CO_2, magenta; CH_4, deep pink) (Köhler et al., 2017), and the areal extent of the Laurentide ice sheet (LIS) relative to the last glacial maximum (dark blue) (Dyke, 2004). (c) Composite aeolian dust strength Z-scores from each dust core region (Fig. 1b), with shading indicating bootstrapped 95% confidence intervals; changes in composite global vegetation cover (green) (Jenny et al., 2019).

To further evaluate and explore the dynamic mechanisms between global temperature and dust, we performed dust sensitivity simulations during the mid- to late-Holocene using the Community Earth System Model (CESM) of the National Center for Atmospheric Research. Specifically, we systematically increased the dust flux from the mid-Holocene (6 ka) to the late-Holocene (PI) to demonstrate the effect of global dust changes on temperatures (Fig. 7). Our simulation showed that, compared with 6 ka, the increase in dust at PI resulted in significant global cooling (especially in the NH), although greenhouse gases also increased from ~265 to ~280 ppm during this period (Fig. 7b and d). Interestingly, the simulation results also show that Holocene temperature changes driven by dust activity on a regional scale (e.g., Eurasia) appear to exhibit spatial differences. This finding aligns with the spatial patterns of Holocene temperature changes over mid-latitude Eurasia demonstrated in previous studies (Jiang et al., 2024), despite the relatively low spatial resolution (Fig. 7). We speculate that this may be attributed to spatial differences in dust activity within the region. Overall, the simulation results are consistent with the observed global dust and temperature reconstructions (Fig. 6), which showed that enhanced dust is correlated with a cooling trend throughout the mid- to late-Holocene. Dust impacts climate through interactions with radiation, clouds, atmospheric chemistry, and other Earth system components (Kok et al., 2023). The radiative effect of many of these interactions are highly uncertain; however, the direct radiative effect of dust is best understood and likely causes a substantial cooling of the order of −0.15 ± 0.35 Wm^{-2} in the present climate (Kok et al., 2023). This cooling occurs primarily because scattering by dust decreases global mean net shortwave radiative flux at the top of the atmosphere (Fig. S4). Increased dust could have thus counteracted greenhouse warming and promoted a decrease in the surface temperature (Fig. 4). However, the simulated cooling in the Northern Hemisphere (~0.2 ℃) is smaller than in the reconstruction (~0.4 ℃) (Figs. 6a and 4b), which may be due to the additional contribution of decreased vegetation cover in the Northern Hemisphere (which was not considered in the simulated experiments of this study) to the cooling trend during the mid- to late-Holocene (Jenny et al., 2019; Tompson et al., 2022). Nonetheless, cooling due to increased dust levels (Kok et al., 2023) could partially explain the reconstructed cooling during the late-Holocene, and thereby help explain the "Holocene temperature conundrum".

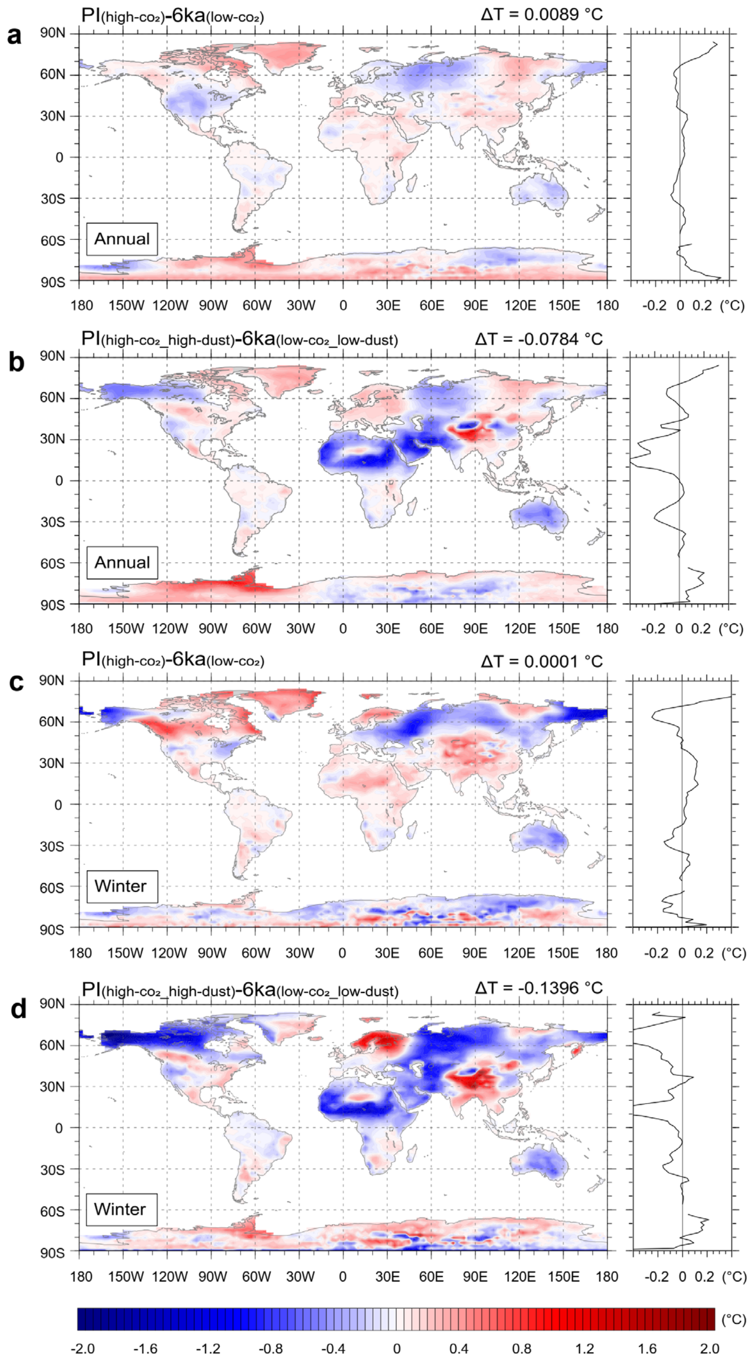

Fig. 7. CESM simulated global temperature changes during the mid- to late-Holocene. Differences in simulated annual (a, b) and winter (c, b) global temperatures between 6 ka and the pre-industrial period. Different colors indicate differences in temperature between 6 ka and the preindustrial period. The zonal mean temperature changes are shown on the right side of each panel.

The relationship between the temperature reconstruction and the various forcing factors can be explained as follows. With little substantive dust forcing during the early- to mid-Holocene (between ~10 and 6 ka BP) (Fig. 6), we suggest that the warming trend in the reconstruction is due to the retreating ice sheets (Liu et al., 2014; Baker et al., 2017). Subsequently, enhanced global dust may have played an important role in the cooling trend after the mid-Holocene. During the mid- to late-Holocene (post-5 ka BP), enhanced dust might have dominated climate forcing, thereby reducing the global mean effective radiative forcing, counteracting greenhouse warming and even resulting in a cooling trend. Although the increase in winter insolation during the mid- to late-Holocene (Laskar et al., 2004) appears inconsistent with the winter cooling trend observed in this study, recent studies suggest that winter temperatures do not respond simply to winter insolation as predicted by climate models (Dong et al., 2022). Instead, changes in summer insolation can trigger a series of complex climatic and environmental impacts—such as monsoon circulation, dust, and vegetation changes (Liu et al., 2016; Bader et al., 2020; Thompson et al., 2022)—which amplify the effects of summer insolation, persist into winter, and offset or even exceed the warming impact of increased winter insolation on winter temperatures. Overall, different temperature trends were caused by differences in the main forcing factors during the early-Holocene and mid- to late-Holocene. This apparent discrepancy between the proxy data and model simulations may be reduced if the cooling trend is interpreted as (partially) due to enhanced dust after ~5 ka BP.

4. Conclusions

In summary, our analyses provide an alternate explanation to the "Holocene temperate conundrum" controversy. Our winter temperature index record highlights the HTM pattern but does not support the Holocene long-term warming trend indicated by model simulations nor does it support the seasonal bias hypothesis. Instead, our composite dust records and simulations suggest enhanced dust during the mid- to late-Holocene was linked to substantial cooling. Our findings further highlight the important effects of dust changes on global climate, which is crucial for predicting future climate change under global warming.

Acknowledgements

This study is jointly supported by the National Natural Science Foundation of China (42488201, 42301175), the National Key Research and Development Program of China (2022YFF0801101), and CAS Youth Interdisciplinary Team (JCTD-2021-05).

Author contributions

X.Z. and S.J. designed the study. S.J., X.Z. and J.F.K. wrote the paper. S.J., X.Z., T.Z., Y.S., L.T. and X.L. collected and analyzed the samples. S.J., L.Y., X.L. and A.C. analyzed the data. Q.L., Z. L. and Y.L. performed the simulation experiments. L.W., W.C., J.P.S. and Z.G. contributed to the discussion of results and manuscript refinement. All authors discussed the results and implications and commented on the manuscript at all stages.

Table 1 List of sites of EAWM (or winter temperature) records used in this study. The winter temperature record is highlighted in bold.

Site No.	Site name	Lat. (°N)	Lon. (°E)	Materials	Age interval (ka BP)	Time resolution (yr per sample)	Dating method	No. of dates	Dating material	Proxy	Reference
1	Huangyanghe	37.42	102.60	Eolian sediment	13.6-0 12.4-0	85 78	^{14}C	8 (a) 17 (b)	Bulk sediment and pollen concentrates	Grain size	Li & Morrill, 2014
2	YX WN2	34.88 34.42	108.75 109.56	Loess	10-0	50	Analogue	5	--	Grain size	Xia et al., 2014
3	GB LGG	34.58 35.76	110.61 107.80	Loess	12-0	10	OSL	50	Bulk sediment	Grain size	Kang et al., 2020
4	Dadiwan section	35.02	105.80	Loess	16-1	30	^{14}C	12	TOC	Zr/Rb	Liu et al., 2020
5	Lake Moon	47.51	120.87	Lake sediment	10.8-0	24	^{14}C	21	Plant macrofossils and bulk sediment	Pinus	Wu et al., 2019
6	Lake Biwa	35.25	136.06	Lake sediment	40-0	109	^{14}C	12	Leaf, Ash, and TOC	Quartz content	Yamada, 2004
7	Huguangyan	21.15	110.28	Lake sediment	14.5-0	177	^{14}C	9	Leaves & bulk sediment	Diatom	Wang et al., 2012
8	MD05-2904	19.46	116.25	Marine sediment	25-0	230	^{14}C & analogue	9	Planktic foraminifer	ΔSST (surface-subsurface)	Steinke et al., 2011
	MD97-2151	8.73	109.87			80	^{14}C	12	Planktic foraminifer		
	18252	9.23	109.38			260	^{14}C	4	Planktic foraminifer		
	MD01-2392 &	9.85	110.21			720	Analogue	3	--		
9	18287	5.65	110.65	Marine sediment	26-0	190	^{14}C	6	Planktic foraminifer	ΔSST	Huang et al., 2011
	17961	8.51	112.33			640	^{14}C	4	Planktic foraminifer		
	17964	6.15	112.20			460	^{14}C	6	Planktic foraminifer		
	MD01-2390	6.64	113.41			220	^{14}C	7	Planktic foraminifer		
10	MD01-2390	6.64	113.41	Marine sediment	21-0	220	^{14}C	7	Planktic foraminifer	ΔSST (surface-subsurface)	Steinke et al., 2010
11	Okinawa Trough	26.07	125.20	Marine sediment	19.2-0	106	^{14}C	10	Planktonic foraminifera	Grain size index	Zheng et al., 2014
12	**Jingchuan section**	**35.25**	**107.72**	**Loess**	**20-0**	**445**	**OSL**	**9**	**Bulk sediment**	**Mollusk**	**Dong et al., 2022**

Table 2 List of sites of dust records used in this study.

No.	Site (Core) name	Lat. (°N/°S)	Lon. (°W/°E)	Materials	Proxy	Reference
North Atlantic region						
1	GGC6	29.21	-43.23	Marine sediment	$^{4}He_{terr}$ and Th	Middleton et al., 2018
2	GC27	30.88	-10.63			
3	GC37	26.82	-15.12			
4	GC49	23.21	-17.85	Marine sediment	^{230}Th	McGee et al., 2013
5	GC66	19.94	-17.86			
6	GC68	19.36	-17.29			
7	ODP-658C	20.75	-18.58	Marine sediment	Terrigenous sediment	deMenocal et al., 2000
8	103GGC	26.07	-78.06	Marine sediment	$^{230}Th_{xs}$	Williams et al., 2016
9	VM20-234	5.33	-33.03			
10	82GGC	4.30	-43.48			
11	55GGC	4.95	-42.93			
12	58GGC	4.75	-43.01	Marine sediment	^{230}Th	Francois et al., 1990
13	21GGC	4.30	-20.25			
14	29GGC	2.51	-19.74			
15	LdRS	37.04	-3.34	Lake sediment	Zr/Th	Jiménez-Espejo et al., 2014
16	TPD	43.45	-7.53	Peat sediment	Elements	Martínez et al., 2019
MiddleEast region						
17	Neor Lae (Neor)	37.96	48.56	Peat sediment	Ti flux	Sharifi et al., 2015
18	Mohos eat bog (MPB)	46.08	25.92	Peat sediment	Lithogenic (K, Si, Ti) elements	Longman et al., 2017
19	SK240485	21.27	68.93	Marine sediment	Nd	Rahaman et al., 2023
20	SK117/GC08	15.50	71.03	Marine sediment	Mg/Al	Mir et al., 2022
21	905	10.40	52.16	Marine sediment	$^{87}Sr/^{86}Sr$	Jung et al., 2004
22	93KL	23.59	64.22	Marine sediment	^{230}Th	Pourmand et al., 2004
23	KL15	12.86	47.43	Marine sediment	$^{230}Th_{xs}$	Palchan et al., 2019
24	KL23	25.75	35.06			
25	MS27PT	31.80	29.46	Marine sediment	Nd, Si/Al	Revel et al., 2015
East Aian region						
26	Tolbo Lake (TB19B)	48.57	90.04	Lake sediment	Grain size	Zhang et al., 2022
27	Yang Chang section (YC)	36.22	81.52	Eolian section	Grain size	Han et al., 2019
28	Lake Gonghai (GH09-B)	38.90	112.23	Lake sediment	Grain size	Chen et al., 2021
29	Hani peatland (HANI)	42.2	126.52	Peat sediment	Rare Earth Elements (REE)	Pratte et al., 2020
30	Lake Xiarinur (XN-A)	42.62	115.47	Lake sediment	Grain size	Xu et al., 2018
31	Western-CLP (W-CLP)	36.72	102.26	Loess section	Accumulation rates	Zhao et al., 2022
32	Desert-loess zone (DLZ)	37.73	109.59			
33	Central-CLP (C-CLP)	35.38	108.57			
34	Southern-CLP (S-CLP)	34.78	109.59			
35	Genggahai Lake (GGH-A)	36.18	100.10	Lake sediment	Grain size	Qiang et al., 2013
36	Lake Barkol (BLK06)	43.64	92.80	Lake sediment	Grain size	Lu et al., 2012
Australa region						
37	Ruined Hut Bog (RHB)	-45.45	169.20	Peat sediment	Trace element	Marx et al., 2009
38	Blue Lake (NC)	-34.43	148.42	Lake sediment	Grain size	Stanley et al., 2002
39	MD03-2611	-35.43	136.10	Marine sediment	kaolinite %	Gingele et al., 2007
40	18460	-8.55	127.85	Marine sediment	ln((Zr+Ti+Fe) /(Al+K))	Kuhnt et al., 2015
41	18479	-12.27	122.31			
42	MD01-2378	-13.10	122.30			
43	Native Companion Lagoon (NCL)	-27.67	153.41	Lake sediment	Trace element	McGowan et al., 2008
44	MD00-2361	-20.08	113.48	Marine sediment	Grain size	Stuut et al., 2014
45	Welsby Lagoon (WEL15-2)	-27.45	153.46	Lake sediment	Elements	Lewis et al., 2020

References

An, Z., Kukla, G., Porter, S. C., & Xiao, J. et al. Late Quaternary dust flow on the Chinese Loess Plateau. *Catena* **18**, 125–132(1991).

Albani, S. et al. Improved dust representation in the Community Atmosphere Model. *J. Adv. Model Earth Sy.* **6**, 541–570 (2014).

Arimoto, R. Eolian dust and climate: relationships to sources, tropospheric chemistry, transport and deposition. *Earth Sci. Rev.* **54**, 29–42 (2001).

Bader, J. et al. Global temperature modes shed light on the Holocene temperature conundrum. *Nat. Commun.* **11**, 4726 (2020).

Badgeley, J., Steig, E. J., & Hakim, G. J. The Holocene Thermal Maximum as an analog for future warming: Insights from paleoclimate data assimilation. In Proceedings of the American Geophysical Union, Fall Meeting 2018, Washington, DC, USA, 10–14 (2018).

Baker, J. L., Lachniet, M. S., Chervyatsova, O., Asmerom, Y., & Polyak, V. J. Holocene warming in western continental Eurasia driven by glacial retreat and greenhouse forcing. *Nat. Geosci.* **10**, 430–435 (2017).

Blaauw, M. & Christen, J. A. Flexible paleoclimate age-depth models using an autoregressive gamma process. *Bayesian analysis* **6**, 457–474 (2011).

Boucher, O. & Tanre, D. Estimation of the aerosol perturbation to the Earth's radiative budget over oceans using POLDER satellite aerosol retrievals. *Geophys. Res. Lett.* **27**, 1103–1106 (2000).

Bova, S., Rosenthal, Y., Liu, Z., Godad, S. P. & Yan, M. Seasonal origin of the thermal maxima at the Holocene and the last interglacial. *Nature* **589**, 548–553 (2021).

Chen, F. et al. Asian dust-storm activity dominated by Chinese dynasty changes since 2000 BP. *Nat. Commun.* **11**, 992 (2020).Chen, S. et al. Holocene dust storm variations over northern China: transition from a natural forcing to an anthropogenic forcing. *Sci. Bull.* **66**, 2516–2527 (2021).

Chen, W., Graf H. & Huang, R. The interannual variability of East Asian winter monsoon and its relation to the summer monsoon. *Adv. Atmos. Sci.* **17**, 48–60 (2000).

Choobari, O. A., Zawar-Reza, P. & Sturman, A. The global distribution of mineral dust and its impacts on the climate system: A review. *Atmos. Res.* **138**, 152–165 (2014).

Cui, S. et al. Inconsistent Hydroclimate Responses in Different Parts of the Asian Monsoon Region during Heinrich Stadials. *Lithosphere* Special 9 (2022).

Curran, M., Morley, A., Wright, J., & Rosenthal, Y. The Holocene Thermal Maximum: A possible analogue for future Ocean-Atmosphere climate Dynamics? In EGU General Assembly Conference Abstracts. 18251 (2018).

deMenocal, P. et al. Abrupt onset and termination of the African Humid Period: rapid climate responses to gradual insolation forcing. *Quat. Sci. Rev.* **19**, 347–361 (2000).

Ding, Y. et al. Interdecadal variability of the East Asian winter monsoon and its possible links to global climate change. *J. Meteorol. Res.* **28**(5), 693–13 (2014).

Dong, Y. et al. The Holocene temperature conundrum answered by mollusk records from East Asia. *Nat. Commun.* **13**, 5153 (2022).

Dyke, A. S. An outline of North American deglaciation with emphasis on central and northern Canada. *Developments in Quaternary Science* **2**, 373–424 (2004).

Fan, Y., & Van den Dool, H. A global monthly land surface air temperature analysis for 1948–present. *J. Geophys. Res.: Atmos.* **113**, D1, (2008).

Francois, R., Bacon, M. P. & Suman, D. O. Thorium 230 profiling in deep-sea sediments: High-resolution records of flux and dissolution of carbonate in the equatorial Atlantic during the last 24,000 years. *Paleoceanogr.* **5**, 761–787 (1990).

Ge, Q. et al. Winter half-year temperature reconstruction for the middle and lower reaches of the Yellow River and Yangtze River, China, during the past 2000 years. *Holocene* **13**, 933–940 (2003).

Gingele, F., De Deckker, P. & Norman, M.Late Pleistocene and Holocene climate of SE Australia reconstructed from dust and river loads deposited offshore the River Murray Mouth. *Earth Planet Sci. Lett.* **255**, 257–272 (2007).

Griffiths, M. L. et al. End of Green Sahara amplified mid-to late Holocene megadroughts in mainland Southeast Asia. *Nat. Commun.* **11**, 4204 (2020).

Han, W. et al. Dust storm outbreak in central Asia after ~3.5 kyr BP. *Geophys. Res. Lett.* **46**, 7624–7633 (2019).

Huang, E., Tian, J. & Steinke, S. Millennial-scale dynamics of the winter cold tongue in the southern South China Sea over the past 26 ka and the East Asian winter monsoon. *Quat. Res.* **75**, 196–204 (2011).

Hurrell, J. W., Hack, J. J., Shea, D., Caron, J. M., & Rosinski, J. A new sea surface temperature and sea ice boundary dataset for the Community Atmosphere Model. *J. Clim.* **21**, 5145–5153 (2008).

Jenny J P et al. Human and climate global-scale imprint on sediment transfer during the Holocene. *Proc. Natl Acad. Sci. USA*, **116**, 22972–22976 (2019).

Jiang, J et al. Spatial patterns of Holocene temperature changes over mid-latitude Eurasia. *Nat. Commun.* ***15***, 1507 (2024).

Jiménez-Espejo, F. J. et al. Saharan aeolian input and effective humidity variations over western Europe during the Holocene from a high altitude record. *Chem. Geol.* **374**, 1–12 (2014).

Jung, S. J. A., Davies, G. R., Ganssen, G. M. & Kroon, D. Stepwise Holocene aridification in NE Africa deduced from dust-borne radiogenic isotope records. *Earth Planet Sci. Lett.* **221**, 27–37 (2004).

Kang, S. et al. Early Holocene weakening and mid- to late Holocene strengthening of the East Asian winter monsoon. *Geology* **48**, 1043–1047 (2020).

Kang, S. et al. Late Holocene anti-phase change in the East Asian summer and winter monsoons. *Quat. Sci. Rev.* **188**, 28–36 (2018).

Kaufman, D. et al. A global database of Holocene paleotemperature records. *Sci. Data* **7**, 115 (2020).

Kaufman, D. S., & Broadman, E. Revisiting the Holocene global temperature conundrum. *Nature* **614**, 425–435 (2023).

Köhler, P., Nehrbass-Ahles, C., Schmitt, J., Stocker, T. F. & Fischer, H. A 156 kyr smoothed history of the atmospheric greenhouse gases CO_2, CH_4, and N_2O and their radiative forcing. *Earth Syst. Sci. Data* **9**, 363–387 (2017).

Kok, J. F. et al. Mineral dust aerosol impacts on global climate and climate change. *Nat. Rev. Earth Environ* **4**, 71–86 (2023).

Kok, J. F. et al. Smaller desert dust cooling effect estimated from analysis of dust size and abundance. *Nat. Geosci.* **10**, 274–278 (2017).

Kuhnt, W. et al. Southern Hemisphere control on Australian monsoon variability during the late deglaciation and Holocene. *Nature Commun.* **6**, 5916 (2015).

Laskar, J. et al. A long-term numerical solution for the insolation quantities of the Earth. *Astronomy & Astrophysics*, ***428***, 261–285 (2004).

Lawrence, D. M., Slater, A. G. & Swenson, S. C. Simulation of present-day and future permafrost and seasonally frozen ground conditions in CCSM4. *J. Clim.* **25**, 2207–2225 (2012).

Lewis, R. J. et al. Insights into subtropical Australian aridity from Welsby Lagoon, north Stradbroke Island, over the past 80,000 years. *Quat. Sci. Rev.* **234**, 106262 (2020).

Li, Y. & Morril, C. Holocene East Asian winter monsoon record at the southern edge of the Gobi Desert and its comparison with a transient simulation. *Clim. Dyn.* **45**, 1219–1243 (2015).

Liu, B., Jin, H. & Yang, F. A late Holocene winter monsoon record inferred from the palaeo-aeolian sand dune in the southeastern Mu Us Desert, northern China. *Sciences in Cold and Arid Regions* **8**, 388–399 (2016).

Liu, X. et al. Centennial-to millennial-scale monsoon changes since the last deglaciation linked to solar activities and North Atlantic cooling. *Clim. Past* **16**, 315–324 (2020).

Liu, X. et al. Late onset of the Holocene rainfall maximum in northeastern China inferred from a pollen record from the sediments of Tianchi Crater Lake. *Quat. Res.* **92**, 133–145 (2019).

Liu, Y. et al. A possible role of dust in resolving the Holocene temperature conundrum. *Sci. Rep.* **8**, 4434 (2018).

Liu, Z. et al. The Holocene temperature conundrum. *Proc. Natl Acad. Sci. USA* **111**, E3501–E3505 (2014).

Liu, Z. et al. Transient simulation of last deglaciation with a new mechanism for Bølling-Allerød warming. *Science*, **325**, 310–314 (2009).

Longman, J. et al. Periodic input of dust over the Eastern Carpathians during the Holocene linked with Saharan desertification and human impact. *Clim. Past* **13**, 897–917 (2017).

Lu, Y. et al. A Holocene dust record in arid central Asia inferred from Lake Barkol, northwest China. *Environ. Earth Sci.* **65**, 213–220 (2012).

Maher, B. A. et al. Global connections between aeolian dust, climate and ocean biogeochemistry at the present day and at the last glacial maximum. *Earth Sci. Rev.* **99**, 61–97(2010).

Mahowald, N. M. et al. Change in atmospheric mineral aerosols in response to climate: Last glacial period, preindustrial, modern, and doubled carbon dioxide climates. *J. Geophys. Res.: Atmos.* **111**, D10202 (2006).

Marcott, S. A., Shakun, J. D., Clark, P. U. & Mix, A. C. A reconstruction of regional and global temperature for the past 11,300 years. *Science* **339**, 1198–1201 (2013).

Martínez Cortizas, A. et al. Holocene atmospheric dust deposition in NW Spain. *Holocene* **30**, 507–518 (2020).

Marx, S. K., McGowan, H. A. & Kamber, B. S. Long-range dust transport from eastern Australia: A proxy for Holocene aridity and ENSO-type climate variability. *Earth Planet Sci. Lett.* **282**, 167–177 (2009).

Mayewski, P. A., & Maasch, K. A. Recent warming inconsistent with natural association between temperature and atmospheric circulation over the last 2000 years. *Clim. Past Discussions*, ***2***, 327-355 (2006).

McGee, D., deMenocal, P. B., Winckler, G., Stuut, J. B. W. & Bradtmiller, L. I. The magnitude, timing and abruptness of changes in North African dust deposition over the last 20,000 yr. *Earth Planet Sci. Lett.* **371**, 163-176 (2013).

McGowan, H. A., Petherick, L. M. & Kamber, B. S. Aeolian sedimentation and climate variability during the late Quaternary in southeast Queensland, Australia. *Palaeogeogr. Palaeoclimatol. Palaeoecol.* **265**, 171–181 (2008).

Meyer, H. et al. Long-term winter warming trend in the Siberian Arctic during the mid- to late Holocene. *Nat. Geosci.* **8**, 122–125 (2015).

Middleton, J. L., Mukhopadhyay, S., Langmuir, C. H., McManus, J. F. & Huybers, P. J. Millennial-scale variations in dustiness recorded in Mid-Atlantic sediments from 0 to 70 ka. *Earth Planet Sci. Lett.* **482**, 12-22 (2018).

Mir, I. A., Mascarenhas, M. B. L. & Khare, N. Geochemistry and granulometry as indicators of paleoclimate, weathering, and provenance of sediments for the past 1, 00,000 years in the eastern Arabian Sea. *J. Asian Earth Sci.* **227**, 105102 (2022).

Neale, R. B. et al. The mean climate of the Community Atmosphere Model (CAM4) in forced SST and fully coupled experiments. *J. Clim.* **26**, 5150–5168 (2013).

Osman, M. B. et al. Globally resolved surface temperatures since the Last Glacial Maximum. *Nature* **599**, 239–244 (2021).

Palchan, D. & Torfstein, A. A drop in Sahara dust fluxes records the northern limits of the African Humid Period. *Nature Commun.* **10**, 3803 (2019).

Paterson, G. A. & Heslop, D. New methods for unmixing sediment grain size data. *Geochemistry, Geophysics, Geosystems* **16**, 4494–4506 (2015).

Porter, S. C. & An, Z. S. Correlation between climate events in the North Atlantic and China during the last Glaciation. *Nature*, 375, 305-308 (1995).

Pourmand, A., Marcantonio, F. & Schulz, H. Variations in productivity and eolian fluxes in the northeastern Arabian Sea during the past 110 ka. *Earth Planet Sci. Lett.* **221**, 39–54 (2004).

Pratte, S. et al. 14 kyr of atmospheric mineral dust deposition in north-eastern China: A record of palaeoclimatic and palaeoenvironmental changes in the Chinese dust source regions. *Holocene* **30**, 492–506 (2020).

Qiang, M. et al. Holocene record of eolian activity from Genggahai Lake, northeastern Qinghai-Tibetan plateau, China. *Geophys. Res. Lett.*, **41**, 589–595 (2014).

Rahaman, W. et al. Eolian versus fluvial supply to the northern Arabian Sea during the Holocene based on Nd isotope and geochemical records. *Geosci. Front.* **14**, 101618 (2023).

Rayner, N. A. A. et al. Global analyses of sea surface temperature, sea ice, and night marine air temperature since the late nineteenth century. *J. Geophys. Res.: Atmos.* **108**, D14 (2003).

Reimer, P.J. et al. 2020. The IntCal20 Northern Hemisphere radiocarbon age calibration curve (0-55 cal kBP). *Radiocarbon* **62**, 725–757 (2020).

Revel, M. et al. 20,000 years of Nile River dynamics and environmental changes in the Nile catchment area as inferred from Nile upper continental slope sediments. *Quat. Sci. Rev.* **130**, 200–221 (2015).

Sassen, K., DeMott, P.J., Prospero, J.M. & Poellot, M.R. Saharan dust storms and indirect aerosol effects on clouds: CRYSTAL-FACE results. *Geophys. Res. Lett.* **30**, 1633 (2003).

Sharifi, A. et al. Abrupt climate variability since the last deglaciation based on a high-resolution, multi-proxy peat record from NW Iran: The hand that rocked the Cradle of Civilization? *Quat. Sci. Rev.* **123**, 215–230 (2015).

Shi, Y. et al. High-Resolution Records of Millennial-Scale East Asian Winter Monsoon in the Shelf Sea of Eastern China. *Geophys. Res. Lett.* **50**, e2022GL102302 (2023).

Stanley, S. & De Deckker, P. A Holocene record of allochthonous, aeolian mineral grains in an Australian alpine lake; implications for the history of climate change in southeastern Australia. *J. Paleolimnol.* **27**, 207–219 (2002).

Steinke, S. et al. Past dynamics of the East Asian monsoon: No inverse behavior between the summer and winter monsoon during the Holocene. *Global Planet. Change,* **78**, 170–177 (2011).

Steinke, S. et al. Reconstructing the southern South China Sea upper water column structure since the Last Glacial Maximum: Implications for the East Asian winter monsoon development. *Paleoceanogr.* **25**, PA2299 (2010).

Stevens, B. Rethinking the lower bound on aerosol radiative forcing. *J. Climate* **28**, 4794–4819 (2015).

Stuut, J. B. W., Temmesfeld, F. & De Deckker, P. A 550 ka record of aeolian activity near North West Cape, Australia: inferences from grain-size distributions and bulk chemistry of SE Indian Ocean deep-sea sediments. *Quat. Sci. Rev.* **83**, 83–94 (2014).

Sun, Y. et al. Influence of Atlantic meridional overturning circulation on the East Asian winter monsoon. *Nat. Geosci.* **5**, 46–49 (2012).

Sun, Y., Lu, H. & An, Z. Grain size distribution of quartz in loess-soil. *Sci. Bull.* **45**, 2094–2097 (2000).Thompson, A. J., Zhu, J., Poulsen, C. J., Tierney, J. E. & Skinner, C. B. Northern Hemisphere vegetation change drives a Holocene thermal maximum. *Sci. Adv.* **8**, eabj6535 (2022).

Wang, B., 2006, The Asian Monsoon: Berlin, Springer Science & Business Media.

Wang, L. et al. The East Asian winter monsoon over the last 15,000 years: its links to high-latitudes and tropical climate systems and complex correlation to the summer monsoon. *Quat. Sci. Rev.* **32**, 131–142 (2012).

Wen, X., Liu, Z., Wang, S., Cheng, J. & Zhu, J. Correlation and anti-correlation of the East Asian summer and winter monsoons during the last 21,000 years. *Nat. Commun.*, **7**, 11999 (2016).

Williams, R. H. et al. Glacial to Holocene changes in trans-Atlantic Saharan dust transport and dust-climate feedbacks. *Sci. Adv.* **2**, e1600445 (2016).

Wu, J. et al. Shrinkage of East Asia winter monsoon associated with increased ENSO events since the mid- Holocene. *J. Geophys. Res.: Atmos.* **124**, 3839–3848 (2019).

Xia, D. et al. Out-of-phase evolution between summer and winter East Asian monsoons during the Holocene as recorded by Chinese loess deposits. *Quat. Res.* **81**, 500–507 (2014).

Xiao, J., Porter, S. C., An, Z., Kumai, H. & Yoshikawa, S. Grain size of quartz as an indicator of winter monsoon strength on the Loess Plateau of central China during the last 130,000 yr. *Quat. Res.* 43(1), 22-29 (1995).

Xiao, J., Zheng, H., & Zhao, H. Variation of winter monsoon intensity on the loess plateau, Central China during the last 130,000 years: evidence from grain size distribution. *The Quat. Res.* **31**, 22–29 (1992).

Xu, B. et al. Decoupling of climatic drying and Asian dust export during the Holocene. *J. Geophys. Res. Atmo.* **123**, 915–928 (2018).

Yamada, K. et al. Last 40 ka climate changes as deduced from the lacustrine sediments of Lake Biwa, central Japan. *Quat. Int.***123**, 43–50 (2004).

Zhang, J. et al. Increasing spring insolation in the Late Holocene intensified aeolian activity in dryland Asia. *Geophys. Res. Lett.*, **49**, e2022GL101777 (2022).

Zhang, W. et al. Holocene seasonal temperature evolution and spatial variability over the Northern Hemisphere landmass. *Nat. Commun.* **13**, 5344 (2022).

Zhang, Y. et al. Asian winter monsoon imprint on Holocene SST changes at the northern coast of the South China Sea. *Geophys. Res. Lett.*, **46**, 13363–13370 (2019).

Zhang., Z., Gong, D., Hu, M., & Lei., Y. Comparisons of the multiple East Asian winter monsoon indices and their relations to climate over eastern China. *J. Satellite Oceanogra. Meteorol.* **1**, 50–60 (2012).

Zhao, S., Xia, D. & Lv, K. Holocene aeolian dust accumulation rates across the Chinese Loess Plateau. *Global Planet. Change* **208**, 103720 (2022).

Zheng, X. et al. ITCZ and ENSO pacing on East Asian winter monsoon variation during the Holocene: Sedimentological evidence from the Okinawa Trough. *J. Geophys. Res.: Oceans.* **119**, 4410–4429 (2014).

Zhou et al. Strengthened East Asian winter monsoon regulated by insolation and Arctic sea ice since the middle Holocene. *Geophys. Res. Lett.*, **50**, e2023GL105440. (2023).

Zhou, X. et al. Time-transgressive onset of the Holocene optimum in the East Asian monsoon region. *Earth Planet Sci. Lett.* **456**, 39–46 (2016).